A Knock-On Deuteron Imager for Measurements of Fuel and Hot-Spot Asymmetry in Direct-Drive Inertial Confinement Fusion Implosions

H. G. Rinderknecht,[1, a)] P. V. Heuer,[1] J. Kunimune,[2] P. J. Adrian,[2] J. P. Knauer,[1] W. Theobald,[1] R. Fairbanks,[1] B. Brannon,[1] L. Ceurvorst,[1] V. Gopalaswamy,[1] C. A. Williams,[1] P. B. Radha,[1] S. P. Regan,[1] M. Gatu Johnson,[2] F. H. Séguin,[2] and J. A. Frenje[2]

[1)] *Laboratory for Laser Energetics, University of Rochester*

[2)] *Plasma Science and Fusion Center, Massachusetts Institute of Technology*

A knock-on deuteron imager (KoDI) has been implemented to measure the hot spot and fuel asymmetry of cryogenic inertial confinement fusion (ICF) implosions on OMEGA. Energetic neutrons produced by D–T fusion elastically scatter ("knock on") deuterons from the fuel layer with a probability that depends on ρR. Deuterons above 10 MeV are produced by near-forward scattering, and imaging them is equivalent to time-integrated neutron imaging of the hot spot. Deuterons below 6 MeV are produced by a combination of sidescattering and ranging in the fuel, and encode information about the spatial distribution of the dense fuel. The KoDI instrument consists of a multi-penumbral aperture positioned 10 to 20 cm from the implosion using a ten-inch manipulator (TIM) and a detector pack at 350 cm from the implosion to record penumbral images with magnification of up to 35×. Range filters and the intrinsic properties of CR-39 are used to distinguish different charged-particle images by energy along the same line of sight. Image plates fielded behind the CR-39 record a 10-keV x-ray image using the same aperture. A maximum-likelihood reconstruction algorithm has been implemented to infer the source from the projected penumbral images. The effects of scattering and aperture charging on the instrument point-spread function are assessed. Synthetic data are used to validate the reconstruction algorithm and assess an appropriate termination criterion. Significant aperture charging has been observed in the initial experimental data set, and increases with aperture distance from the implosion, consistent with a simple model of charging by laser-driven EMP.

I. INTRODUCTION

Three-dimensional perturbations are often significant in inertial confinement fusion (ICF) implosions at stagnation, limiting their performance.[1,2] When low-mode asymmetries are present in the stagnated fuel layer, the implosion kinetic energy is not efficiently converted to hot-spot pressure, and regions with low areal density (ρR) reduce the confinement time.[3] Measurements of the ρR using down-scattered neutrons demonstrate spatial variations,[4] but higher spatial resolution is needed to understand and control the source of these asymmetries.

Despite the importance of converged fuel symmetry for successful ICF implosions, diagnosing the converged fuel is challenging for direct-drive implosions at the Omega Laser Facility. Compton scattering of high-energy x rays for converged-fuel radiography is under development at the National Ignition Facility (NIF); however, the need for >40 keV x rays and multiple lines-of-sight for 3-D reconstruction makes this challenging from both a source and detector standpoint.[5] Imaging of scattered neutrons (6 to 12 MeV) records angularly resolved information on the areal density of a region of the converged shell depending on neutron energy.[6] The present neutron imaging diagnostics, however, require expensive apertures, limiting the number of available lines of sight. Activation detectors on the NIF encode the local fuel areal density in the fluence of high-energy neutrons observed in each direction,[1] but achieving sufficiently high precision using this technique requires higher yields than are produced in OMEGA implosions.

The same scattering process that produces the down-scattered neutrons also generates a population of forward-scattered ("knock-on") deuterons and tritons. While these charged particles are stopped by the hohlraum in indirect drive experiments, in directly driven ICF they escape, carrying information that can be used to diagnose the cold fuel morphology. Imaging of charged particles produced in ICF implosions with ∼100% efficiency is a well-developed technology that uses solid-state detectors and is convenient for implementation on multiple lines of sight.[7,8]

In this manuscript, we describe the design of a penumbral imaging camera to record knock-on deuteron images (KoDI) and co-aligned x-ray images from direct-drive cryogenic implosions on OMEGA. Section II presents the theory of (n,d) production by implosions and discusses what information is encoded in the images. Section III describes the design of the KoDI instrument, including the model of the aperture response and effects of aperture charging. In Section IV we discuss the image reconstruction algorithm used, including tests of the termination condition and the effective resolution using numerical studies. Section V presents preliminary data from OMEGA cryogenic implosions. We conclude with an overview of the results and a discussion of future directions for this work in Section VI.

[a)] hrin@lle.rochester.edu

II. SCATTERING THEORY

Near peak convergence of the fuel, deuterium–tritium fusion in the hot spot produces energetic neutrons ($E_{\rm n} \approx$ 14.1 MeV) that propagate out of the hot spot. Most neutrons escape the fuel; however, a fraction scatter from deuterium and tritium ions. The cross sections for elastic deuteron [$\sigma_{\rm d(n,n)d}$] and triton [$\sigma_{\rm t(n,n)t}$] scattering are approximately 0.64 and 0.93 barns, respectively, at the peak neutron energy of 14.1 MeV. The probability of neutron scattering $P_{\rm n}$ is given by

$$P_{\rm n} = 1 - \exp\left[-\left(\sigma_{\rm n,d} f_{\rm d} + \sigma_{\rm n,t} f_{\rm t}\right) \frac{\rho R_{\rm fuel}}{\langle m_{\rm fuel}\rangle}\right], \quad (1)$$

where f_j is the number fraction of ion species j in the fuel, $\sigma_{\rm n,j}$ is the total cross-section for neutron interaction with a given ion species, and $\langle m_{\rm fuel}\rangle$ is the mean ion mass in the fuel. (For pure deuterium-tritium fuel, $f_{\rm t} = 1 - f_{\rm d}$ and $\langle m_{\rm fuel}\rangle = f_{\rm d} m_{\rm d} + f_{\rm t} m_{\rm t}$.) This total neutron scattering probability is the sum of the scattering probability from each species, $P_{\rm n} = P_{\rm n,d} + P_{\rm n,t}$.[9] The probability $P_{\rm n,d}$ that the neutron elastically scattered a deuteron is then

$$P_{\rm n,d} = \frac{\sigma_{\rm d(n,n)d} f_{\rm d}}{\sigma_{\rm n,d} f_{\rm d} + \sigma_{\rm n,t} f_{\rm t}} P_{\rm n}. \quad (2)$$

For typical values of areal density ($\rho R_{\rm fuel} < 1$ g/cm^2), the exponential term is much less than unity ($\lesssim 0.19$) and the probability of scattering is approximately linear with ρR. Assuming an equimolar D:T ratio, the probability for elastically scattering of a deuteron (triton) is approximately 7.7×10^{-5} (1.12×10^{-4}) per mg/cm^2 of areal density, respectively. In a typical OMEGA directly driven cryogenic implosion, which produces 10^{14} D–T fusion neutrons and has assembled fuel areal density of the order of 100 mg/cm^2, $\sim 10^{12}$ scattered deuterons are expected to be produced.

As a two-body reaction, conservation of energy and momentum fully constrain the kinematics of elastic scattering, and the energy of the scattered particle is fully determined by the scattering angle. Defining ϕ as the scattering angle in the center-of-mass reference frame and assuming the initial velocity of the scattered particle in the laboratory frame is negligible, the forward angle of the scattered particle in the laboratory frame is $\theta = (\pi - \phi)/2$, and its energy is

$$E_{j,\rm lab} = 4\cos^2\theta \frac{m_j m_{\rm n}}{\left(m_j + m_{\rm n}\right)^2} E_{\rm n0}. \quad (3)$$

The maximum energy of a scattered deuteron (triton) is then 8/9 (3/4) of the incident neutron energy, or approximately 12.5 (10.6) MeV, respectively.

The probability of scattering also varies with scattering angle: differential cross sections $\partial P/\partial(\cos\phi)$ are reported in the nuclear data repository ENDF.[10,11] The probability of scattering into an angle θ is calculated from these values by translating into the laboratory frame:

$$\frac{\partial P}{\partial \theta} = 4\cos\theta \sin\theta \frac{\partial P}{\partial(\cos\phi)}. \quad (4)$$

The scattered particle energy and probabilities for elastic deuteron and triton scattering as a function of laboratory scattering angle are shown in Fig. 1.

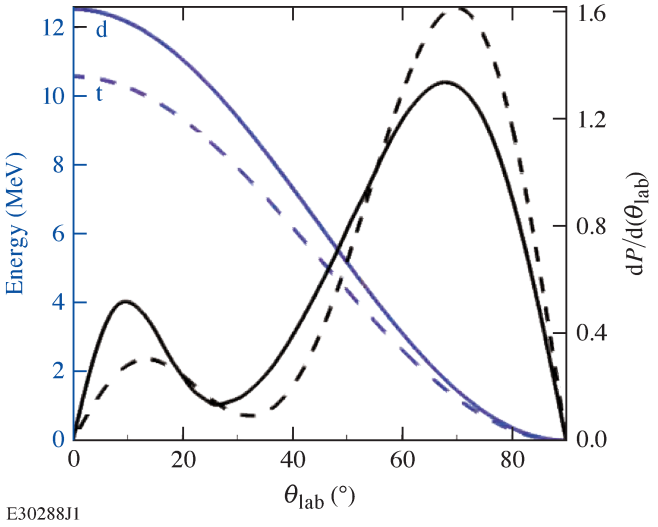

FIG. 1. Scattered particle energy (blue curves) and probability of scattering into a given laboratory angle θ (black curves) for deuterons (solid) and tritons (dashed).

When diagnosing an implosion, the scattering angle is defined by the position of the scattering event relative to the axis defined by the neutron source and the diagnostic aperture. Consider the simplified case of a point neutron source surrounded by a uniform spherical fuel mass. In this case, the scattering angle is the angle between the detector axis and the scattering position, and the energy of the observed particle corresponds directly to its birth location relative to the detector axis. Furthermore, since scattering probability scales linearly with $\rho R_{\rm fuel}$ and the differential cross section for scattering is known, the number of particles observed from a given energy or radius can be used to infer areal density at that scattering angle.

The finite size of the neutron source, thickness of the assembled fuel, and the ranging of the scattered particles as they escape the implosion are encoded in images of the particles recorded at different energies. The highest energy deuterons (above 12 MeV) must be produced by small-angle scattering (<15°), and must be produced near the outer edge of the implosion to avoid energy losses to ranging. Images of the high-energy deuterons, therefore, represent an image of the neutron source convolved with a slight blur caused by the scattering angle. Lower-energy deuterons (below 6 MeV) are produced by two processes: direct large-angle scattering (>45°) from the

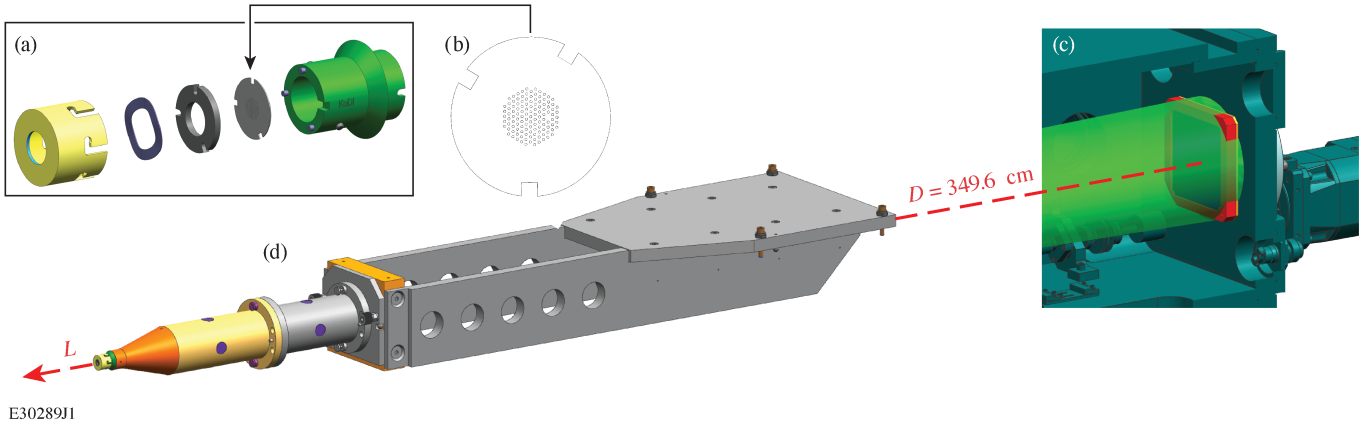

FIG. 2. Schematic of the KoDI instrument. (a) Contents of the nose tip assembly, from left to right: nose cap, wave spring, spacer, multi-penumbral pinhole array, and nose tip. (b) Schematic of multi-penumbral pinhole array design: 200 to 300-μm-diameter holes laser drilled in hexagonal close-packed array. (c) Detector assembly held at the rear of the TIM (red) and signal coverage (green). (d) Pre-existing Proton Core Imaging System (PCIS) hardware used to hold aperture assembly.

outside of the fuel, and ranged-down deuterons produced deeper in the fuel. Images of lower-energy deuterons, therefore, encode the location and density of the assembled fuel mass. By discriminating deuteron energy in the images, information about the shape of the hot spot and of the surrounding cold fuel can be obtained.

III. INSTRUMENT DESIGN

The KoDI instrument is a high-magnification penumbral imaging camera for charged particles and x rays that can be fielded on OMEGA using the ten-inch–manipulator (TIM) diagnostic platform. The instrument hardware is shown in Fig. 2. The pre-existing proton core imaging system (PCIS)[8,12,13] is used to field an aperture at a configurable distance 10 to 20 cm from target chamber center (TCC). A detector pack is fielded at the rear of the TIM, at a distance $D = 349.6$ cm from TCC. The detector pack is attached to a custom holder flange that is bolted to the rear of the TIM in place of the rear window. The insertion depth of the aperture (L) is limited by the cryogenic shroud, and varies based on the angle of each TIM with respect to the shroud axis, as shown in Table I. In practice magnifications ($M \equiv D/L$) up to $M = 35$ are used.

The detector pack contains range filters, a 10-cm-square sample of the nuclear track detector CR-39 to record the charged particles, and two BAS-SR image plates to record images using >10 keV x-rays. Charged particles incident on the CR-39 leave trails of molecular damage; etching the exposed sample in sodium hydroxide causes these damage trails to produce conical "tracks" that are visible using a microscope. The diameter of tracks is dependent on the etch time and the stopping power of the particles in the material, and therefore depends on the particle species and incident energy. For particles above 1 MeV, the diameter of the resulting track decreases monotonically with energy, creating a diameter-energy relationship for each species.[14–16] Tracks must have a diameter larger than 2 μm to be observed reliably. This limits the energy range of particles that are detected, and sets an upper limit of the order of 10^6 tracks per cm^2 fluence, above which tracks cannot be measured because of significant overlap.[17] This fluence limitation is the primary reason the detector pack distance from the implosion was increased in the KoDI design.

TABLE I. Minimum KoDI insertion depth (L) and maximum magnification (M) for each TIM.

TIM	1	2	3	4	5	6
Min(L) (cm)	9.19	17.33	13.88	9.19	8.19	9.20
Max(M)	38.0	20.2	25.2	38.0	42.7	38.0

An example of CR-39 and x-ray data recorded on an implosion is shown in Fig. 3. Differential filtering is used to distinguish between high- and low-energy deuteron populations. The left half of the CR-39 is filtered by 135-μm tantalum, transmitting only deuterons initially above 10 MeV. The right half is filtered by 10-μm tantalum, transmitting deuterons initially above 2 MeV.[18] The diameter of tracks is used to further discriminate the data into rough energy bins to interpret the images. While the exact diameter-energy relationship varies from sample to sample and is not known *a priori*, the energy order and approximate energy range can be inferred. The analysis of the x-ray data is described in Ref. 19.

Penumbral imaging was selected to maximize the statistics of the recorded signal. The information is encoded in the penumbral region of the projected apertures. For aperture radius R_a and source radius R_s, each aperture projects a circle with radius R_aM and penumbral half-width $R_s(M - 1)$. For penumbra in a hexagonal

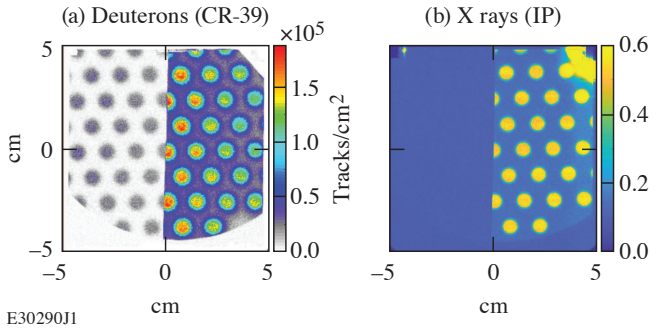

FIG. 3. Example of recorded data: (a) deuteron fluence recorded using CR-39; (b) x-ray fluence (PSL/pixel) recorded using image plates. Detectors are differentially filtered to record high- and low-energy deuterons: 135-μm Ta (left); 10-μm Ta (right).

close-packed array with separation S, the unit cell area is $A = S^2\sqrt{3}/2$. To avoid overlap of neighboring penumbra we further require that $R_a + R_s < S/2$. In this case, the average penumbral track density is bounded by

$$n_p \equiv \frac{N_p}{A} \lesssim \frac{Y}{2\sqrt{3}D^2}\left[\frac{R_a R_s}{(R_a+R_s)^2}\right]\left(\frac{M-1}{M}\right) \qquad (5)$$

for deuteron yield Y. For a fixed fluence on the detector ($F \propto Y/D^2$), maximizing the statistics of the signal is obtained by maximizing the second term, which occurs for a matched aperture and object radius ($R_a = R_s$), and by fielding a sufficiently large aperture array to cover the detector plane with signal. For the initial experiments we have used apertures with radius 100 to 150 μm to ensure a clear separation between neighboring images.

The resolution of the resulting image can be assessed as the distance required to observe a significant change in the penumbral brightness. Assuming the primary uncertainty is statistical, a "significant difference" would be one equal to the local statistical uncertainty $\sigma_N = \sqrt{N}$. The average gradient in the penumbra is estimated as $N/R_s(M-1)$. Further assuming that the resolution in the reconstructed source (Δx_s) scales as the demagnified image resolution ($\Delta x_i/(M-1)$), we can assess the resolution scaling to be:

$$\frac{\Delta x_s}{R_s} \approx \sqrt{\frac{D}{R_s(M-1)}}\left(\frac{Y\#_a}{4\pi}\right)^{-1/4}, \qquad (6)$$

where $\#_a$ is the number of apertures used. This form highlights the importance of a high magnification and large signal. For our detector geometry and deuteron yields of 10^{12}, fractional resolutions of better than 10% are expected.

A. Aperture response

Two effects cause the point-spread function (PSF) of the penumbral apertures to differ from the ideal knife edge: charged-particle scattering in the substrate and electrical charging of the array.

Each penumbral aperture is made by laser drilling a 200 μm-thick tantalum or 175 μm-thick tungsten substrate, which are thick enough to stop the highest energy deuterons produced by the implosion. This process produces a conical hole with an opening angle of about 10°. Unlike x-ray imaging, for which attenuation of signal at the edge produces the PSF, charged particles traversing solid material both lose energy and accumulate scattering angle (straggle). The substrate thickness was selected to range out all (n,d) and (n,t) particles not passing through the apertures, but particles near the edge are transmitted with reduced energy and added straggle. Because of the high magnification of the camera, the detector pack subtends only 1.2° half-angle with respect to the aperture, so even a small amount of straggle is sufficient to remove all structure and produce a uniform background. Using the stopping and range in matter (SRIM) code,[20] we determined that passing through only 10 μm of tungsten is sufficient for the deuteron signal to lose all apparent structure. Despite the effects of scattering, the edge of the PSF is extremely sharp (~1 μm). A Monte Carlo calculation using the straggling and ranging model confirmed this result and indicated the contrast at the edge exceeds 10^{-3} for all deuteron energies of interest.

Electrical charging of the aperture array produces a more significant effect and has been observed previously using the PCIS system.[21,22] Assuming small-angle deflections, the relationship between a particle's position in the aperture plane r_a and in the image plane r_i can be derived assuming a radial electric field E in the aperture plane acting over a fixed length Δz. The electric field is estimated semi-analytically as the field due to an infinite plate of charge containing a circular hole, and scales linearly with the charge density Q [that is, $E(r_a) = QE'(r_a)/2\pi\epsilon_0$]. The shape of the electric-field function in the aperture is shown in Fig. 4(a). In normalized units ($r'_a = r_a/R_a$, $r'_i = r_i/R_aM$) and with the particle kinetic energy K, the function describing the effect of the electric field on particle trajectories is:

$$r'_i = r'_a + \frac{e\Delta z}{4\pi\epsilon_0}\left[\frac{Q}{K}\frac{D}{R_a}\frac{M-1}{M^2}\right]E'(r'_a). \qquad (7)$$

The point-spread function is calculated as the derivative of this function: PSF $= [\mathrm{d}r'_i/\mathrm{d}r'_a]^{-1}$. We can see immediately that the charged-aperture PSF is a family of curves that depends only on the value of a coefficient $V \equiv \left[QD(M-1)/KR_aM^2\right]$. The shape of the PSF as a function of this coefficient is calculated semi-analytically and is shown in Fig. 4(b). [Throughout this manuscript, we select $\Delta z = 200$ μm and V has units of (Coulomb/cm^2)/MeV.]

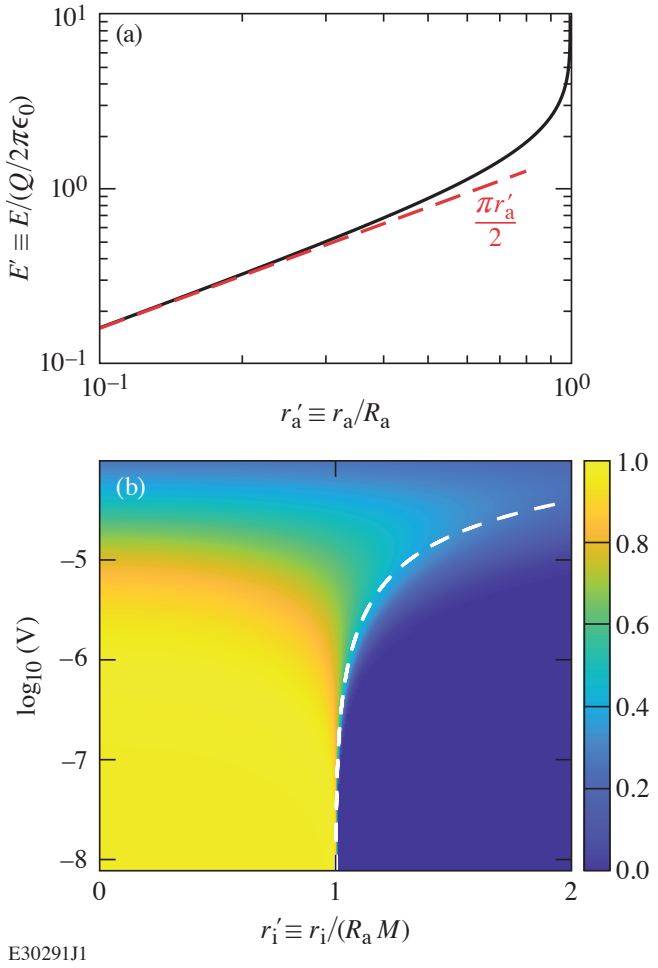

FIG. 4. (a) Electric field inside a circular array (black curve), linear asymptote (red line). (b) Semi-analytical point-spread functions for charged-particle imaging with a circular aperture including the effects of aperture charging; (dashed white curve) radius at 50% of peak intensity.

Charging effects appear to be negligible for values $V \lesssim 10^{-7}$, but become dominant for $V \gtrsim 3 \times 10^{-5}$. For accurate reconstructions using a charged aperture, the amount of charging must be known and the blurring caused by charging effects must not dominate the structure caused by the object. The PSF radius at 50% of maximum [dashed white curve in Fig. 4(b)] increases monotonically with the charging coefficient, so the amount of charging can be inferred *in situ* from the data by comparing the projected radius of the deuteron aperture images with x-ray measurements of the camera magnification. It is worth noting that V depends on particle energy, and low-energy deuterons are more susceptible to the effects of charging than high-energy deuterons.

IV. IMAGE RECONSTRUCTION

The images of the source are encoded in the recorded penumbral images, and a numerical technique must be employed to recover them. This can be considered numerically as an unknown source vector $\vec{S}$ convolved with a known encoding matrix $\vec{\vec{T}}$ to produce the measured vector $\vec{P}$, that is, $\vec{S} \cdot \vec{\vec{T}} = \vec{P}$. To solve this problem we employ the iterative reconstruction algorithm described by Gelfgat *et al.* in the limit of Poisson statistics.[23]

The transfer matrix $\vec{\vec{T}}$ is calculated using the semi-analytical PSF model, known aperture geometry, camera magnification measured from the x-ray data, and charging coefficient inferred using the average deuteron penumbral image radius. Transfer matrices are calculated as 4-D matrices, with dimensions corresponding to $[x, y]$ location in the source and image planes. The spatial resolution of the source and image plane are matched such that $\delta\vec{x}_S \approx \delta\vec{x}_P M$ in order to achieve the maximum resolution in the reconstruction. The deuteron tracks may be binned as desired prior to reconstruction, so ultimately the achievable resolution is limited by statistics, as suggested by Eq. (6). In practice, the transfer matrices are on the order of 10^3 to 10^4 pixels in the source plane and 10^5 to 10^6 pixels in the image plane, and require several tens of GB to store. Often only a subset of the matrix is used in a reconstruction.

For the reconstruction algorithm, the source and image data are represented as 1-D vectors and the transfer matrix is reshaped into a 2-D matrix. A uniform background is included by adding an additional source pixel with uniform projection over the image plane. A uniform prior is used, and is iteratively updated to maximize the likelihood function $\mathcal{L}$. The nonconstant part of the log-likelihood is $\log \mathcal{L} = N \sum_i f_i \log p_i$, for N total tracks, $f_i = N_i/N$ the normalized signal in an image pixel, and $p_i = \sum_j s_j T_{ji}$ the normalized expected signal in each pixel at each step of the iteration. To increase numerical stability and enforce positivity in the solution, the step size is reduced from the suggested value in Ref. 23 by a factor of 3, and proposed negative- or zero-valued pixels at each step are replaced with values that asymptote to zero.

A. Termination condition

The reconstruction algorithm converges to a maximum likelihood over a number of iterations that depends on the source size and number of tracks in the image. Numerical testing shows that the required number of iterations to reach convergence generally grows as $N^{0.3-0.35}$ for a fixed image size. The asymptotic reconstructions generally appear to be overfit, by concentrating numerical noise into high variations between neighboring pixels. To avoid overfitting, identifying a condition for when to terminate the reconstruction algorithm is desirable. According to Wilks' theorem, the likelihood ratio

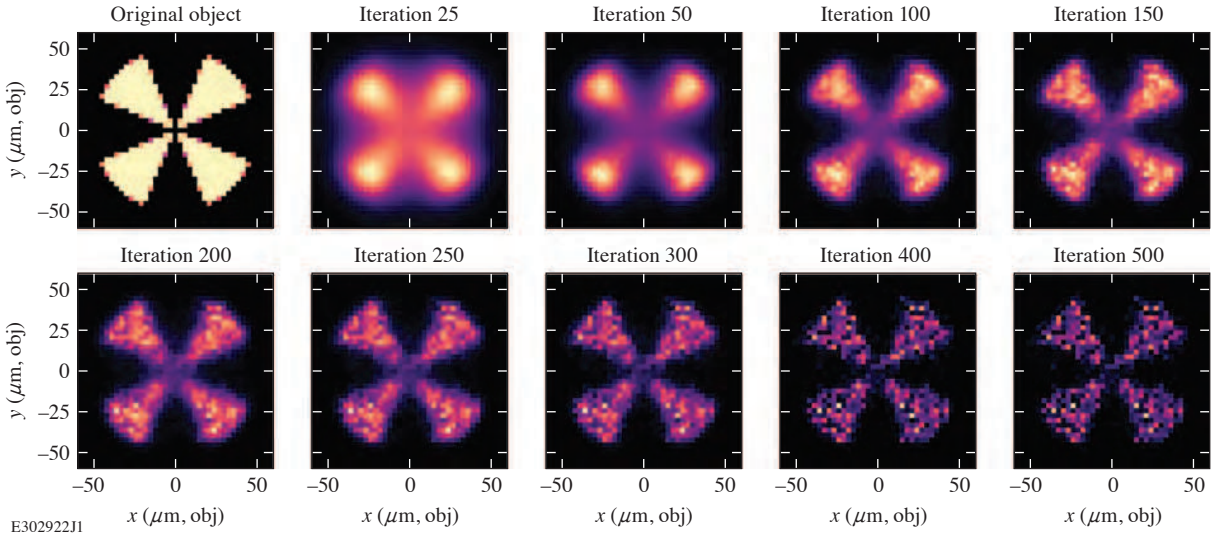

FIG. 5. Images from different iterations during the reconstruction of a synthetic KoDI dataset. The original object is shown in the upper left panel.

$\lambda_i \equiv -2\left[\log(\mathcal{L}_i) - \log(\mathcal{L}_\infty)\right]$ will trend to a χ^2 probability distribution with degrees of freedom equal to the number of free parameters (i.e. source pixels) as the number of samples becomes large.[24] However, only source pixels that carry significant information contribute to this distribution. An intuition for this fact can be obtained from the definition of the log-likelihood: for small pixel values ϵ, the contribution to the log-likelihood is $\lim_{\epsilon\to 0} \epsilon \log(\epsilon) \to 0$, and variation in near-zero-valued pixels in the object do not significantly affect the value of $\log(\mathcal{L})$. An "effective" degrees of freedom ($\mathrm{DOF}_{\mathrm{eff}}$) must therefore be used to infer the expected distribution in the likelihood ratio.

Presently, we have defined a termination condition using the likelihood ratio as follows. The reconstruction algorithm is run until the asymptotic value is approached. For each step of the reconstruction, a likelihood ratio λ_i is calculated with respect to the final iteration. The effective degrees of freedom is calculated from the normalized pixel values of the asymptotic source $s_j = S_j / \sum_j S_j$ as:

$$\mathrm{DOF}_{\mathrm{eff}} = \sum_j^J \frac{s_j}{s_j + J^{-1}}, \tag{8}$$

where J is the number of pixels in the source. This sigmoid-type function ascribes significance to pixels that contain signal greater than a uniform baseline. The termination criterion C_i for each iteration step is then defined in terms of the cumulative χ^2 distribution as: $C_i = 1 - \chi^2_{\mathrm{cdf}}(\lambda_i, \mathrm{DOF}_{\mathrm{eff}})$, and the first iteration such that $C_i < 0.5$ is selected.

Assuming Wilks' theorem applies and the degree-of-freedom metric in Eq. (8) is sufficiently accurate, this approach prevents overfitting or underfitting by selecting a reconstruction step that is consistent with the median value of the expected likelihood ratio distribution. Preliminary numerical studies suggest the "significance" of a pixel depends on the statistics in the recorded image, and further study of this termination condition is merited.

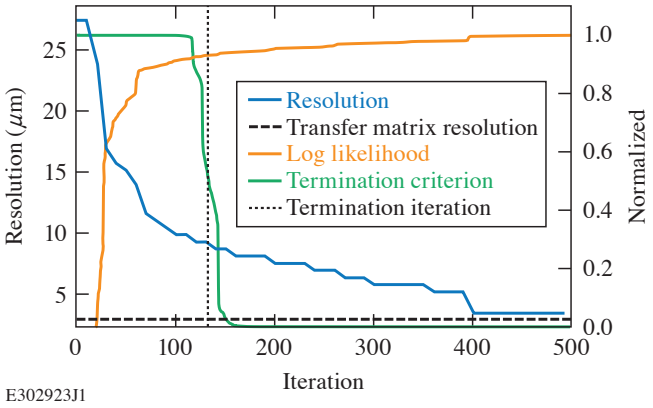

FIG. 6. The estimated spatial resolution (blue curve), log-likelihood (orange curve) and termination criterion (green curve) as a function of iteration number for the reconstruction from synthetic data shown in Fig. 5. The log-likelihood is normalized from iteration 20 to 500 for display. (dashed black line) The spatial resolution of the transfer matrix used for the reconstruction. (dotted black line) The optimal termination iteration selected by the termination criterion.

B. Numerical studies

A synthetic KoDI diagnostic is used to validate the reconstruction algorithm described above. Synthetic data are created in two steps. First, a deuteron-probability distribution is created in the detector plane by multiplying a given source image by the transfer matrix. Then,

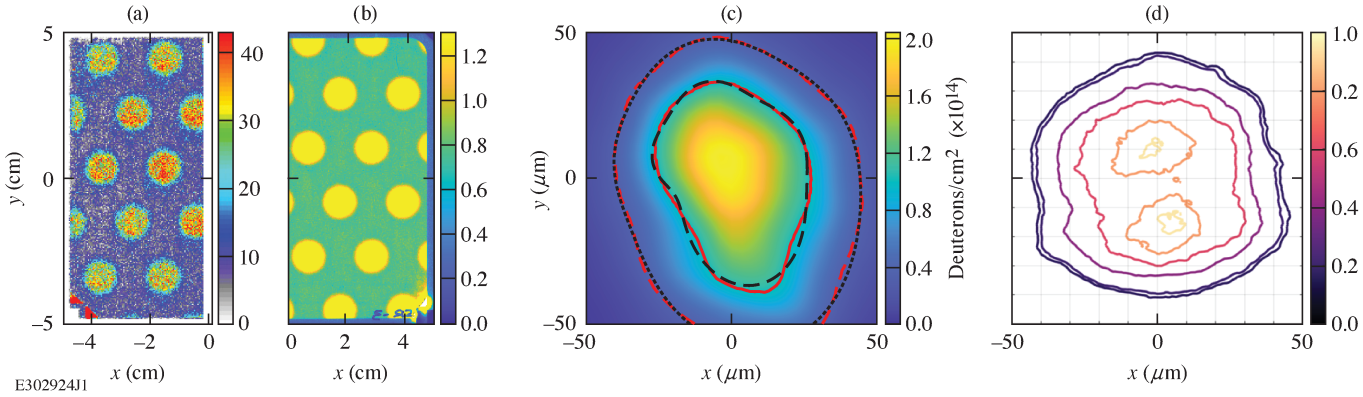

FIG. 7. KoDI data recorded on OMEGA cryogenic implosion 102568. (a) High-energy deuteron image (> 10 MeV, tracks per 400-μm square pixel); (b) 10-keV x-ray image (PSL per 100-μm square pixel); (c) reconstructed deuteron source with 50% and 17% intensity contours (red) and Legendre polynomial fits to order 4 (black); and (d) reconstructed x-ray source.

deuteron positions drawn from this image distribution as well as a uniform distribution (representing background noise) are combined and analyzed using the same reconstruction algorithm as applied to the experimental data. Figure 5 shows images reconstructed from a synthetic data set (created using the object shown in the upper left panel) at different iterations of the reconstruction algorithm. The synthetic image was sampled using 5×10^6 total deuterons, 20% of which were drawn from a uniform background distribution. The source plane was 80-μm square with a pixel size of approximately 3 μm, while the image plane was 5×10 cm (i.e., one half of the CR-39 detector) with 70-μm square pixels. At early iterations (25 to 50) the data are underfit, while at later iterations (300 to 500) overfitting results in noise. The similarity between the images in the range 100 to 200 highlights the need for an objective termination criterion to select an iteration in this range as the final reconstruction. Application of the termination criterion described above selects iteration #133 from this reconstruction series.

Synthetic KoDI data can also be used to estimate the spatial resolution of the reconstructed images. The resolution of an image reconstructed from synthetic data is estimated by convolving the true object with a series of progressively wider Gaussian kernels and comparing the resulting array to the reconstructed image using a χ^2 test. The resolution is then defined as the full-width-at-half-maximum value of the Gaussian kernel that minimizes the χ^2 metric. Figure 6 shows that, for the same reconstruction shown in Fig. 5, the resolution improves monotonically throughout the reconstruction and asymptotically approaches the resolution of the transfer matrix, while the log-likelihood increases monotonically. The effective resolution of the reconstruction is therefore limited by the termination criterion. The present termination criterion (#133, resolution 9.3±0.6 μm) appears to coincide with the beginning of noise growth (visible in step #150), but is possibly earlier than ideal because the sharp edges of the test source continue to resolve better at later steps. In general, data with higher signal levels will terminate later, allowing a greater resolution to be reached. For the example presented here with 5×10^6 deuterons, the effective spatial resolution at termination is estimated to be ∼10 μm. Future work will use synthetic data to investigate the dependence of resolution on statistics, as well as assess different termination criteria.

V. INITIAL RESULTS

The KoDI system was fielded on a series of direct-drive cryogenic implosions on OMEGA during 2021 and 2022. In the majority of the experiments, the diagnostic was fielded in TIM-1 with a magnification of 25 or 35. In one shot series (102560–102571), multiple KoDI instruments were fielded at different magnifications on each shot.

Figure 7 shows the (a) deuteron and (b) x-ray data recorded on shot 102568. Analysis of the raw x-ray data indicated a magnification of 35.70±0.10. The deuteron data were analyzed to infer a charge-induced magnification increase of 5.4±0.3%. These values were used to calculate the point-spread function for reconstructing the data. A reconstruction of a high-energy deuteron image is shown in Fig. 7(c), and the corresponding reconstructed x-ray image in Fig. 7(d). The inferred shape and size of the hotspot is comparable between the x rays and deuterons. The 50% radius (P0) of the deuteron image was fit as 30 μm, with a significant mode-2 (P2/P0) of 30%. The axis of the mode-2 matches that seen in the reconstructed x-ray image. The camera was fielded in TIM-5, observing the implosion nearly perpendicularly to the stalk axis, and the observed mode-2 is elongated in the stalk direction.

Aperture charging was observed on the majority of the experiments. Figure 8 shows the ratio of the deuteron projected aperture radius to the x-ray-inferred value, which was typically 1.05 and was significantly greater than 1 on almost all experiments. Experiments fielded in different TIM's appeared to produce systematically

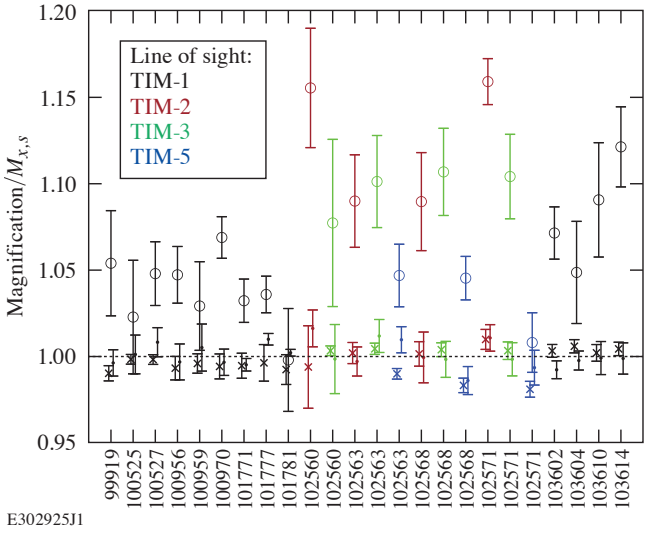

FIG. 8. Ratio of magnification inferred from (x) x-ray projected aperture radius, (·) deuteron aperture separation, and (○) deuteron aperture radius to value inferred from x-ray aperture separation. Colors indicate the detector fielding position.

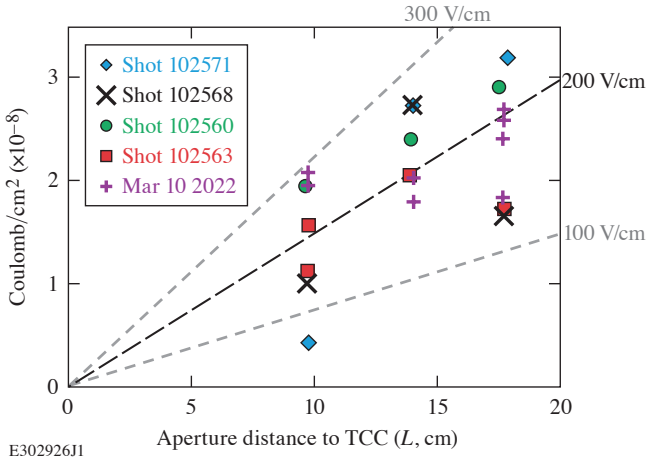

FIG. 9. Aperture charging inferred from high-energy deuteron images recorded on a series of experiments with KoDI fielded at various insertion depths. Data from Mar 10, 2022 (+) were all recorded in TIM-1. Predictions from the EMP charging model [Eq. (10)] (dashed lines).

different values in the inferred magnification, suggesting that the aperture distance from TCC affected the amount of charging observed.

The inferred charging from two shot series in which the magnification was varied is shown in Fig. 9, and appears to show increased charging with aperture distance from TCC. Multiple points at the same distance and campaign are produced by analyzing images with different deuteron energies. In the first series (102560–102571), the aperture distance was associated with which TIM was used to field the instrument (shown in Fig. 8). To break the degeneracy between the aperture distance and the detector line of sight, the instrument was fielded at various distances on a single line of sight (TIM-1) on a second campaign (Mar 10 2022, +). This series confirmed that charging is constant or increasing with distance. Neither result can be explained by a charging source that originates at TCC and is prompt with respect to the deuterons, such as absorption of hot electrons or ionization by x rays; these sources would be expected to reduce with the square of the distance.

The observed trend is roughly consistent with a model in which the electromagnetic pulse (EMP) radiation produced by the laser–target interaction drives currents in the TIM body. The highest energy deuterons travel at 0.11× the speed of light, such that they reach the aperture at 10 cm (18 cm) at 2.9 ns (5.2 ns) after the laser drive, respectively. During this time differential, the outward-propagating EMP encompasses a greater volume of the diagnostic TIM. Assuming the potential on the diagnostic grows linearly with interaction time and the capacitance of the aperture approximates that of a single circular plate ($C \approx 8\epsilon_0 R_a$), then we derive the following static model for the aperture charge:

$$Q = \frac{8\epsilon_0}{\pi R_a} E_{\rm EMP} L \left(\frac{1}{\beta} - 1\right) \tag{9}$$

$$\approx Q_0 \frac{L}{R_a} \left(\frac{E_{\rm EMP}}{\rm V/cm^2}\right) \left[21.6\sqrt{A}\left(\frac{K}{\rm MeV}\right)^{-\frac{1}{2}} - 1\right] \tag{10}$$

where β is the relativistic velocity, $Q_0 = 2.25 \times 10^{-13}$ C/cm^2 and A is the ion mass in amu. Using this model, an EMP electric-field amplitude $E_{\rm EMP}$ of the order of 100 V/cm is roughly consistent with the data. This value is in agreement with a prediction for the magnitude of the EMP fields produced by OMEGA.[25] This model is likely to be oversimplified, since it neglects the time-dependent electrical response of the instrument body and the power spectrum and wavelength of the EMP. However, interpretation of low-energy deuteron images will likely require a substantial reduction or elimination of aperture charging, and the EMP hypothesis provides guidance regarding what future modifications to the diagnostic will be necessary to achieve this goal.

VI. CONCLUSIONS AND FUTURE WORK

In summary, a TIM-based high-magnification penumbral imaging camera has been designed to record knock-on deuteron images from direct-drive cryogenic ICF implosions on OMEGA. Fusion neutrons scatter deuterons with energy correlated to scattering angle, such that high-energy deuterons encode the shape of the fusing hot spot and low-energy deuterons encode the shape of the surrounding dense fuel. The KoDI instrument is designed to record both high- and low-energy deuteron images using a multi-penumbral array and CR-39 detector with differential Ta range filter, as well as high-energy (10-keV) x-ray images using image plates on the same line of sight. Depending on the line of sight used, KoDI

can record images with magnification up to 35 and predicted resolutions better than 10%. The effect of aperture charging on the point-spread function was observed in the majority of data recorded, and is accounted for using a semi-analytical model. Reconstruction of the source image from the recorded penumbral images is accomplished using an iterative maximum likelihood algorithm. The reconstruction algorithm was tested using synthetic data, and a termination condition for the reconstructions was proposed using the likelihood ratio and an effective degree-of-freedom measure calculated from the reconstructed source. Initial data have been collected on a series of experiments. Increased aperture charging was observed for experiments with greater aperture distance to the implosion. A simple EMP model was developed that accounts for the trend and order of magnitude of the aperture charging.

While the model of aperture charging presented here is, in principle, sufficient to interpret the diagnostic data, in practice, the reduction or elimination of aperture charging will significantly benefit the experiments by reducing analysis error and maximizing camera resolution. Several approaches to controlling the aperture charging are being investigated, informed by the EMP charging model presented here. These include replacing a significant portion (the front 30 cm) of the diagnostic snout with a nonconductive material; fabricating the aperture from a nonconductive material such as silicon dioxide processed using nanolithography techniques; and reducing the EMP source by changing the target mounting stalk.[26] These solutions will be tested in upcoming campaigns to assess their effects on the recorded data.

The data recorded by the KoDI diagnostic will enable detailed studies of the hot spot and assembled cold fuel on OMEGA. Comparisons of the high-energy deuteron and x-ray images will be used to infer the profiles of temperature and density to localize mix in the hot spot.[27] The details of cold-fuel distribution will be inferred by comparison of experimental and simulated KoDI images that take into account the charged-particle scattering and ranging in the implosion. Up to six lines of sight will be used to reconstruct the 3-D profiles of neutron emission and cold dense fuel. This data will provide unprecedented constraints on fuel assembly in direct-drive implosions, which will assist in the goals of reaching improved symmetry and hydro-equivalent ignition conditions on OMEGA.

ACKNOWLEDGMENTS

This material is based upon work supported by the Department of Energy National Nuclear Security Administration under Award Number DE-NA0003856, the University of Rochester, and the New York State Energy Research and Development Authority. The support of DOE does not constitute an endorsement by DOE of the views expressed in this paper.

This report was prepared as an account of work sponsored by an agency of the U.S. Government. Neither the U.S. Government nor any agency thereof, nor any of their employees, makes any warranty, express or implied, or assumes any legal liability or responsibility for the accuracy, completeness, or usefulness of any information, apparatus, product, or process disclosed, or represents that its use would not infringe privately owned rights. Reference herein to any specific commercial product, process, or service by trade name, trademark, manufacturer, or otherwise does not necessarily constitute or imply its endorsement, recommendation, or favoring by the U.S. Government or any agency thereof. The views and opinions of authors expressed herein do not necessarily state or reflect those of the U.S. Government or any agency thereof.

[1] H. G. Rinderknecht, et al., *Phys. Rev. Lett.* 124, 145002 (2020).
[2] D. T. Casey, et al., *Phys. Rev. Lett.* 126, 025002 (2021).
[3] O. A. Hurricane, et al., *Phys. Plasmas* 29, 012703 (2022).
[4] O. M. Mannion, et al., *Phys. Plasmas* 28, 042701 (2021).
[5] G. N. Hall, et al., *Rev. Sci. Instrum.* 87, 11E310 (2016).
[6] D. T. Casey, et al., *Rev. Sci. Instrum.* 87, no. 11, p. 11E715, 2016.
[7] F. H. Séguin, et al., *Phys. Plasmas* 13, 082704 (2006).
[8] F. H. Séguin, et al., *Phys. Plasmas* 23, 032705 (2016).
[9] Note that the derivation of Eq. 1 assumes total neutron loss after an interaction. In principle, multiple neutron scattering will modify the spectrum of elastically-scattered particles.
[10] M. B. Chadwick, et al., *Nucl. Data Sheets* 107, 2931 (2006).
[11] ENDF differential cross-sections are reported as a function of the inverse cosine angle, $\cos\phi_{\mathrm{ENDF}} = -\cos\phi$.
[12] F. H. Séguin, et al., *Rev. Sci. Instrum.* 75, 3520 (2004).
[13] J. L. DeCiantis, et al., *Rev. Sci. Instrum.* 77, 043503 (2006).
[14] F. H. Séguin, et al., *Rev. Sci. Instrum.* 74, 975 (2003).
[15] N. Sinenian, et al., *Rev. Sci. Instrum.* 82, 103303 (2011).
[16] B. Lahmann, et al., *Rev. Sci. Instrum.* 91, 053502 (2020).
[17] A. Zylstra, et al., *Nucl. Instrum. Methods Phys. Res., Sect. A* 681, 84 (2012).
[18] The 10 μm Ta filter blocks the high flux of 'ablator' protons with energy typically below 1.0 MeV.[14].
[19] P. J. Adrian, et al., *Rev. Sci. Instrum.* 92, 043548 (2021).
[20] J. F. Ziegler, et al., *Nucl. Instrum. Methods Phys. Res., Sect. B* 268, 1818 (2010).
[21] H. G. Rinderknecht, PhD thesis, Massachusetts Institute of Technology (2015).
[22] J. H. Kunimune, et al., *Phys. Plasmas* 29, 072711 (2022).
[23] V. I. Gelfgat, et al., *Comput. Phys. Commun.* 74, 335 (1993).
[24] S. S. Wilks, *Ann. Math. Stat.* 9, 60 (1938).
[25] A. Poyé, et al., *Phys. Rev. E* 92, 043107 (2015).
[26] P. Bradford, et al., *High Power Laser Sci. Eng.* 6, E21 (2018).
[27] A. Pak, et al., *Phys. Rev. Lett.* 124, 145001 (2020).

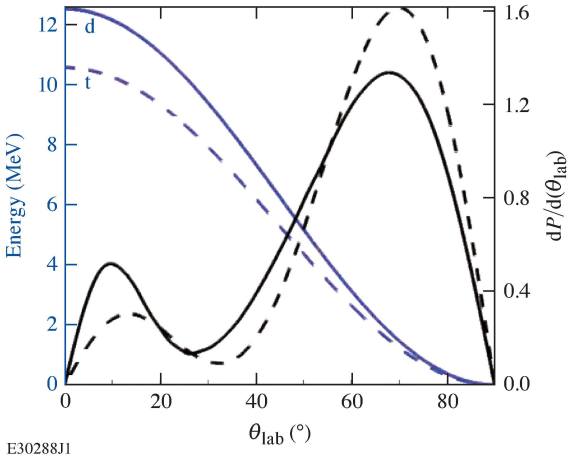
d
t
Energy (MeV)
θ_{lab} (°)
$dP/d(\theta_{lab})$
0
2
4
6
8
10
12
0
20
40
60
80
0.0
0.4
0.8
1.2
1.6
E30288J1

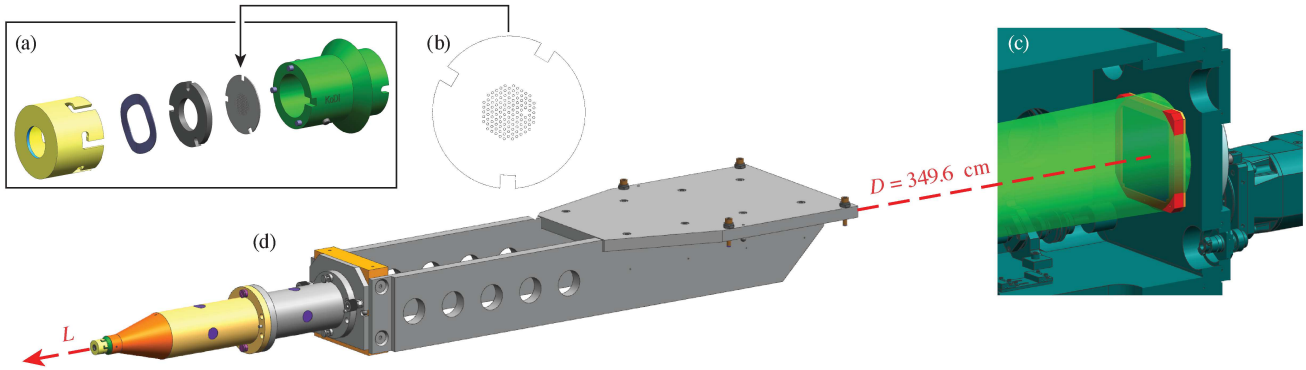
(a)
(b)
(c)
(d)
D = 349.6 cm
L
E30289J1

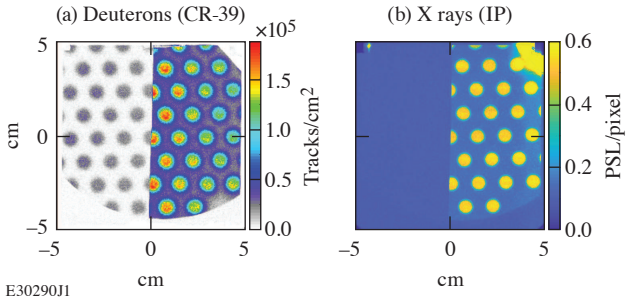
(a) Deuterons (CR-39)
(b) X rays (IP)
×10^5
1.5
1.0
0.5
0.0
Tracks/cm^2
0.6
0.4
0.2
0.0
PSL/pixel
5
0
–5
cm
–5
0
5
cm
E30290J1

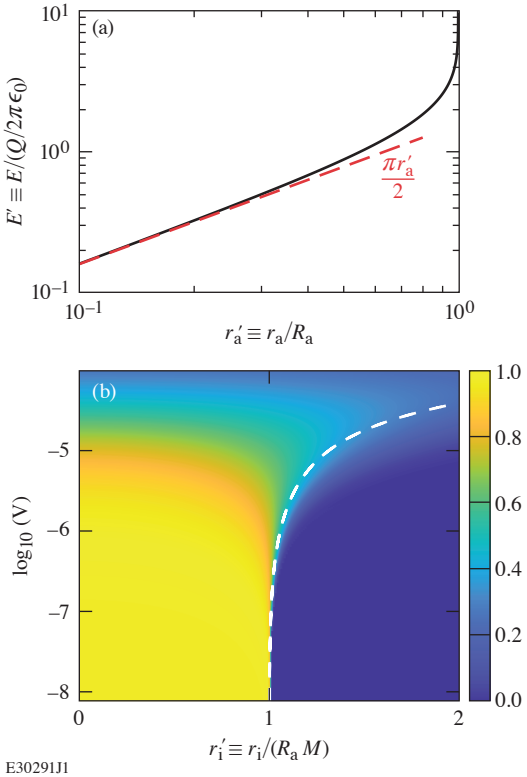
(a)
10^1
10^0
10^{-1}
10^{-1}
10^0
$E' \equiv E/(Q/2\pi\epsilon_0)$
$r'_a \equiv r_a/R_a$
$\frac{\pi r'_a}{2}$
(b)
−5
−6
−7
−8
0
1
2
$\log_{10}$ (V)
$r'_i \equiv r_i/(R_a M)$
1.0
0.8
0.6
0.4
0.2
0.0

E30291J1

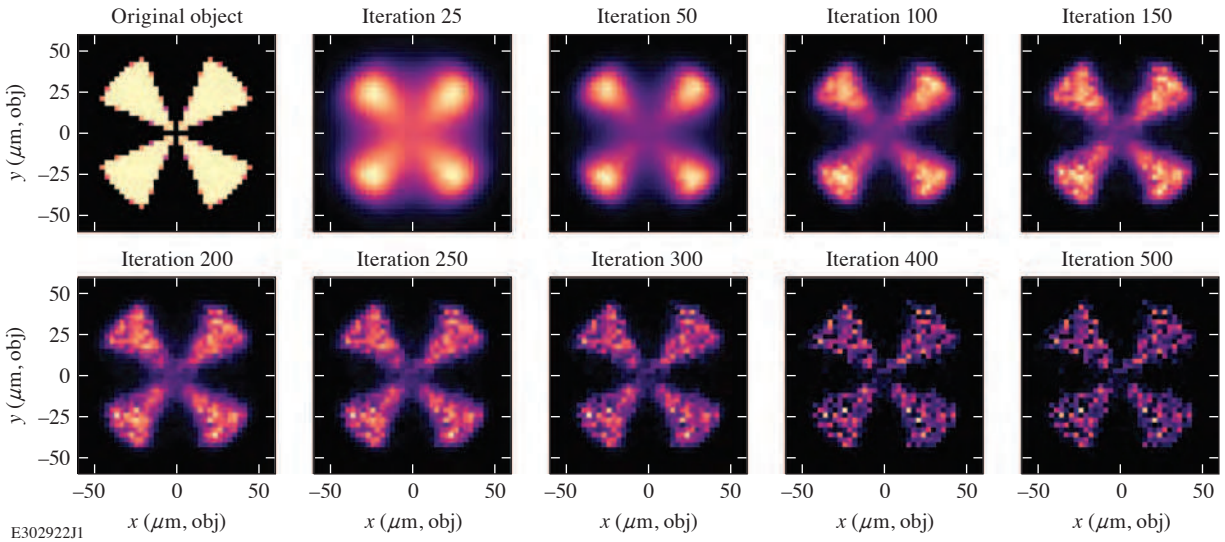
Original object
Iteration 25
Iteration 50
Iteration 100
Iteration 150
Iteration 200
Iteration 250
Iteration 300
Iteration 400
Iteration 500
y (μm, obj)
x (μm, obj)
50
25
0
–25
–50
E302922J1

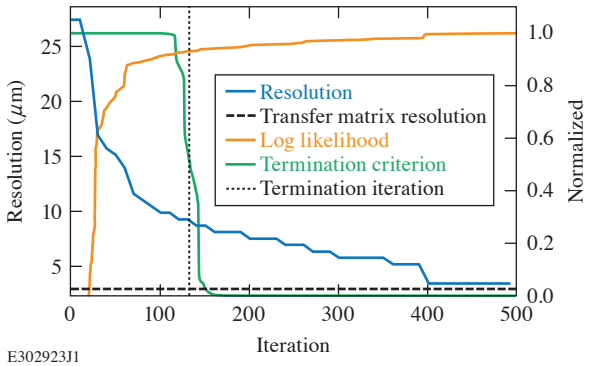
Resolution (μm)
25
20
15
10
5
0
100
200
300
400
500
Iteration
1.0
0.8
0.6
0.4
0.2
0.0
Normalized
Resolution
Transfer matrix resolution
Log likelihood
Termination criterion
Termination iteration

E302923J1

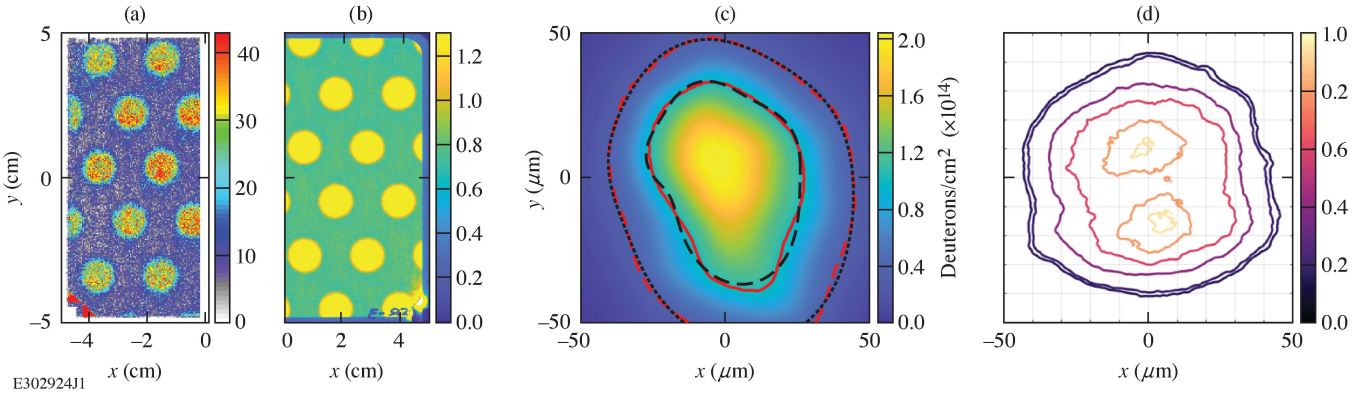
(a)
(b)
(c)
(d)
y (cm)
x (cm)
y (μm)
x (μm)
Deuterons/cm² (×10¹⁴)
E302924J1

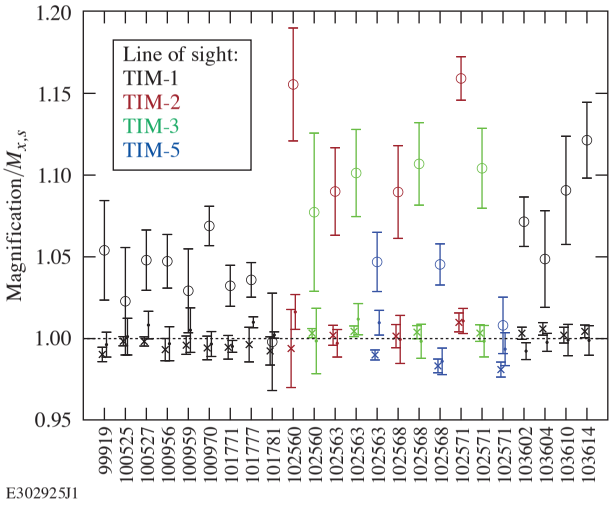
Line of sight:
TIM-1
TIM-2
TIM-3
TIM-5
Magnification/$M_{x,s}$
1.20
1.15
1.10
1.05
1.00
0.95
99919
100525
100527
100956
100959
100970
101771
101777
101781
102560
102560
102563
102563
102563
102568
102568
102568
102571
102571
102571
103602
103604
103610
103614
E302925J1

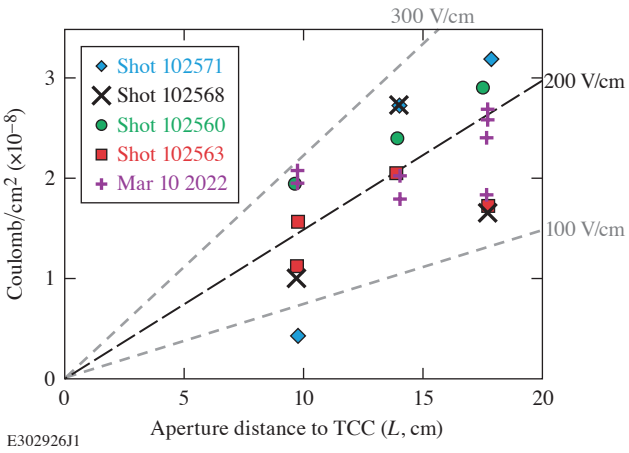
300 V/cm
200 V/cm
100 V/cm
Shot 102571
Shot 102568
Shot 102560
Shot 102563
Mar 10 2022
Coulomb/cm^2 ($\times 10^{-8}$)
Aperture distance to TCC (L, cm)
0
1
2
3
0
5
10
15
20
E302926J1